Site-dependent numerical safety analysis in microwave skin spectroscopy: comparison of monopole and vivaldi antennas

Shangyang Shang and Milica Popović*

Department of Electrical and Computer Engineering, McGill University, Montreal, QC, Canada

Over the past decade, sensors for skin cancer detection, with operation at micro- and millimeter-wave frequency range, have been under investigation. Thus, safety concerns related to radiation exposure have become critical, especially for patients with vulnerable skin. Studies to date fell short in detailed safety assessments. Many evaluations rely on a single-tissue model representing a single anatomical site. Moreover, most studies assess safety solely via specific absorption rate (SAR) but omit the temperature-rise analysis induced by radiation exposure. In this work, we investigate two types of surface-wave-based antennas operating in the microwave band. Multilayer tissue models were constructed to emulate nine major body sites. The key safety metrics, including the SAR distribution and temperature increase, were analyzed through full-wave electromagnetic simulations in Ansys HFSS. The results reveal substantial inter-site variability in the metrics, highlighting the necessity of full-body evaluation prior to determining the overall safety measures for the new diagnostic devices. Furthermore, we derive power limits for surface-wave antennas in accordance with U.S. and Canadian safety standards, and verify their conservativeness via temperature analysis. Our findings provide a basis for a comprehensive framework for radiation safety assessment of wearable devices operating in the microwave band.

KEYWORDS

radiation safety, thermal effect, specific absorption rate, skin cancer detector, microwave

1 Introduction

Skin cancer is one of the most prevalent malignancies worldwide (Roky et al., 2025). In recent years, microwave and millimeter sensing techniques have emerged as promising tools for non-invasive skin cancer diagnosis (Naqvi et al., 2025). These methods utilize the dielectric contrast between malignant and healthy tissues, allowing tumor detection without surgical intervention (Wu and Liu, 2024). These approaches are non-ionizing, painless, low-cost, and capable of providing real-time diagnostic information (Schiavoni et al., 2023). Recent advances in micro-/mm-wave systems have further improved spatial resolution and enhanced contrast between tissue types (Mirzaee et al., 2021). In parallel, deep learning techniques have been increasingly applied to signal processing, significantly improving diagnostic reliability (Costanzo et al., 2023). Efforts have also been made to develop compact sensor systems, aiming to facilitate clinical integration and point-of-care deployment (Naqvi et al., 2024).

Despite their clinical potential, safety challenges remain a critical concern for the skin cancer detectors. In the close-contact scenarios, electromagnetic (EM) energy is coupled into the superficial layers, and most of the absorption occurs in the epidermis and dermis (Suryanata et al., 2023), particularly within high-water-content cutaneous appendages (Haider et al., 2022). Previous studies have shown that at anatomical sites where a low-water-content layer (e.g., fat) is sandwiched between high-water-content tissues (e.g., skin and muscle), standing-wave and impedance-matching effects can arise, leading to a significant increase of local SAR within the skin layer (Christ et al., 2006). Although these micro-/mm-wave-based systems medical typically operate at low power levels, attention must be paid to radiation exposure and its physiological effects. In particular, patients with skin cancer may have vulnerable skin at the lesion site, making them more susceptible to EM heating (Alemaryeen and Noghanian, 2023). Exposure safety limits have accordingly been established by national and international standards such as the U.S. Federal Communications Commission (FCC) guidelines (Fields, 1997) and IEEE C95.1 and ICNIRP (Bailey et al., 2019), which confine the localized SAR to 1.6 W/kg over 1 g of tissue.

Previous studies have extensively investigated EM radiation safety by analyzing the interactions between electromagnetic waves and biological tissues at various body sites (Kodera et al., 2024; Sacco et al., 2022). However, in the field of detectors for skin cancer diagnosis, most previous studies have rarely evaluated the radiation safety of their designs. Even in the studies including such safety discussion, SAR analysis were often conducted on one tissue model representing a single body site, such as the forearm or abdomen (Kaur et al., 2024; Kaur et al., 2022). These approaches fail to account for the substantial anatomical differences in skin and subcutaneous tissue structures across various body sites. Such anatomical variations significantly influence the electric field distribution and, consequently, the SAR pattern, especially at microwave and millimeter-wave frequencies. As a result, safety assessments based on a single anatomical site may not accurately reflect the actual risks posed during clinical deployment.

An additional limitation of prior studies is the lack of consideration for tissue temperature rise under the exposure. This issue is not confined to skin cancer detection systems but is also present in many researches on wearable micro-/mm-wave devices. Although SAR is the primary metric codified in current safety guidelines, emerging devices with unconventional radiation patterns and scanning schemes may lie outside the assumptions underlying those frameworks. By contrast, temperature rise is the direct physiological factor associated with thermal tissue damage and provides a more comprehensive characterization of thermal effects by integrating factors not captured by SAR, e.g., exposure duration, tissue perfusion, and heat diffusion properties. Accordingly, temperature rise should be incorporated as a complementary indicator in radiation safety evaluation.

This work aims to address the missing studies in radiation safety assessment for skin-cancer-detection sensors and other wearable micro-/millimeter-wave devices. Although this broader term is used, our experiments and analyses are confined to the microwave band. Safety-related radiation metrics were obtained through full-wave EM simulations conducted in Ansys HFSS. Nine multilayer tissue models were constructed to represent the skin and subcutaneous structures at different body sites, including the sole, thigh, buttock, abdomen, palm, arm, neck, and leg. Each model was scanned by two generations of surface-wave antennas developed for skin cancer diagnosis: the Vivaldi antenna (latest design) and the monopole antenna (initial design). To evaluate conservative worst-case scenarios, we focused on three key metrics: peak electric field intensity, peak SAR, and peak temperature rise. The results reveal substantial variation across body sites for all three metrics, confirming the necessity of multi-site modeling in safety evaluations. Furthermore, we observed notable discrepancies between peak SAR and peak temperature rise across sites, underscoring the importance of including both metrics in comprehensive safety analysis. Power limits for each antenna were derived from the SAR results to ensure compliance with the strictest US and Canada standards, and then validated through temperature-rise analysis, demonstrating their effectiveness in maintaining thermal safety.

2 Method and materials

2.1 Surface-wave method for skin cancer diagnosis

Cancerous lesions such as basal cell carcinoma, squamous cell carcinoma, and melanoma typically contain a higher water content than healthy skin tissues (Gniadecka et al., 2003). As a result, these tumors exhibit higher dielectric permittivity, particularly in the microwave frequency bands (Schiavoni et al., 2023). The local EM response varies depending on the presence or absence of a tumor.

In the surface-wave-based sensing approach, two antennas are placed in contact with the skin surface. One acts as a transmitter (Tx) and the other as a receiver (Rx). These antennas are designed to excite and detect EM surface waves that are confined to propagate along the skin–air interface. In comparison to healthy skin, the presence of a cancerous lesion introduces greater attenuation and phase shift between the Tx and Rx antennas. Larger tumor sizes generally enhance these contrast effects. In practical measurements, the transmission coefficient parameter, S_{21}, is found to be a feasible indicator of both amplitude reduction and phase delay, reflecting the underlying tissue changes. A detailed theoretical model of this surface-wave sensing mechanism is provided in our recent work (Shang et al., 2025).

2.2 Antenna structures

Two types of surface-wave-based antennas were used in this study to evaluate radiation safety for skin cancer sensing: Vivaldi antennas and monopole antennas, as illustrated in Figure 1. Their designs have been reported in our previous works (Mokhtari and Popović, 2025; Bahramiabarghouei et al., 2015). They were selected in this study as their operation in the desired frequency range is optimized for direct on-skin placement.

The Vivaldi antennas, shown in Figure 1A, represent the latest surface-wave-based design tailored for skin cancer diagnosis. The antennas are fabricated on a 50-μm-thick flexible Kapton substrate (relative permittivity $\varepsilon_r = 3.4$, loss tangent $tan\delta = 0.008$). The substrate provides flexibility and offers bio-compatibility,
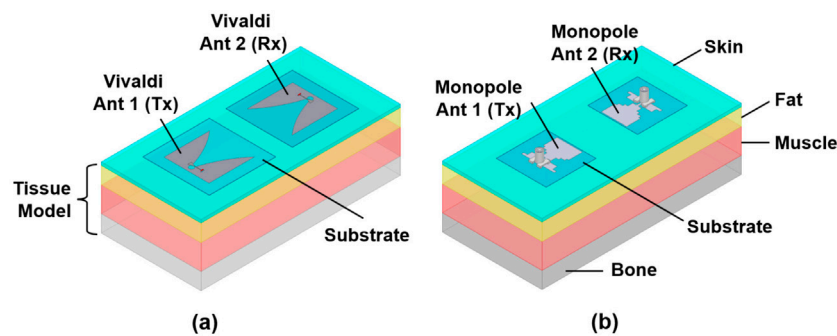
FIGURE 1
Antenna pairs operated on multi-layer tissue models: **(a)** the Vivaldi antennas; **(b)** the monopole antennas.
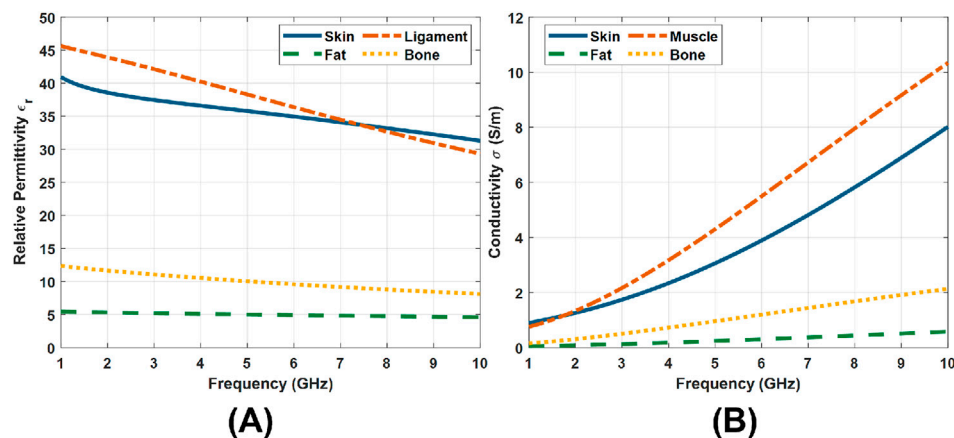

FIGURE 2
Dielectric properties of tissue layers from 1 GHz to 10 GHz (IFAC – CNR, 2024). **(A)** Relative permittivity. **(B)** Conductivity.

ensuring good contact with the skin surface without compromising safety or comfort. Their working frequency band is from 3 GHz to 6 GHz. Each antenna measures 26 mm × 17 mm. The Vivaldi structure was selected due to its end-fire radiation pattern and wide bandwidth, enabling better energy confinement along the skin surface. Owing to the high permittivity of biological tissue, the antenna is much smaller than its conventional free-space counterpart. The detailed design process and numerical simulation results of the Vivaldi antenna are provided in (Mokhtari and Popović, 2025), where its effectiveness in indicating both the horizontal and vertical dimensions of skin lesions is demonstrated.

The monopole antenna (Figure 1B) are the initial version of the surface-wave-based antennas. Originally proposed in (Bahramiabarghouei et al., 2015), they have the same flexible Kapton substrate as the monopole antennas. Each monopole antenna measures 20 mm × 20 mm and operates in the 2–5 GHz band. A standard SMA connector is attached on the reverse side to enable stable and repeatable measurements. Previous studies have demonstrated its strong surface-wave radiation and functionality in skin lesion characterization through simulations (Shang et al., 2024) and experimental validation (Shang et al., 2025).

2.3 Biological tissue models

As illustrated in Figure 1, the tissue models consist of multiple layers arranged from the surface inward: skin, fat, muscle, and bone. Here, a single-skin layer is used because the wavelengths associated with the selected frequency bandwidths are unlikely to resolve individual layers of the skin. The dielectric dispersions of the four tissue layers from 1 GHz to 10 GHz are shown in Figure 2, with data obtained from (IFAC – CNR, 2024). The thermal properties for each layer were adopted from the IT'IS database (IT'IS Foundation, 2025). A total of nine models were constructed to represent the tissues under test at different body sites, including the abdomen, arm, buttock, forehead, leg, neck, palm, sole, and thigh. In the forehead, palm, and sole models, all four layers are included. For the remaining six models, the bone layer was excluded, as the soft tissue thickness at these sites exceeds 20 mm. In this case, EM waves operating in the 2–6 GHz band attenuate significantly before reaching the bone, making its inclusion unnecessary for accurate simulation.

All models were built in Ansys HFSS. They share identical lateral dimensions, with a length of 12 cm and a width of 6 cm, providing a surface area large enough to accommodate the selected antennas,

TABLE 1 Tissue layer thicknesses by body site.

Tissue layer	Abdomen	Arm	Buttock	Forehead	Leg	Neck	Palm	Sole	Thigh
Skin (mm)	1.3	1.0	1.7	0.9	1.1	1.5	1.4	1.6	1.2
Fat (mm)	4.7	3.0	12.1	1.3	2.8	1.5	0.3	0.4	5.7
Muscle (mm)	20	20	20	2.9	20	20	9.6	14.3	20
Bone (mm)	-	-	-	8.5	-	-	8.0	4.8	-

which feature compact structures and low spatial requirements. The detailed configurations and thicknesses of each tissue layer are provided in Table 1. The skin and fat thicknesses were obtained from (Lee and Hwang, 2002; Störchle et al., 2018), respectively. For the forehead, the muscle and bone thicknesses were referenced from (Choi et al., 2019; Rowbotham et al., 2023). Similarly, for the palm and sole, the corresponding values were taken from (Morimoto et al., 2017; Morgan et al., 1967; Angin et al., 2014; Griffin and Richmond, 2005). In the remaining six body site models, the muscle layer was uniformly set to 20 mm. Although the actual muscle thickness in these regions is typically greater, this simplification improves computational efficiency. Given that the EM wave penetration depth in soft tissue at 2–6 GHz is less than 20 mm (IFAC – CNR, 2024), this assumption does not compromise the accuracy of the simulation results.

2.4 Radiation safety analysis

The antennas and multilayer tissue models were designed and simulated using Ansys HFSS, in which both EM field analysis and radiation safety evaluation were performed. For the monopole antenna, the frequency sweep was conducted from 2 GHz to 5 GHz with a step size of 0.1 GHz. For the Vivaldi antenna, the sweep range was set from 3 GHz to 6 GHz with the same step size.

Microwave exposure safety is commonly evaluated using two thermally relevant indicators: the SAR and the induced tissue temperature rise. SAR quantifies the rate at which EM energy is absorbed by biological tissues, expressed in watts per kilogram (W/kg). Both Canada and the United States have established strict regulatory limits. According to Health Canada's Safety Code 6 and the U.S. FCC guidelines (Demers et al., 2014; Fields, 1997), the peak spatial-average SAR must not exceed 1.6 W/kg, averaged over 1 g of tissue. Tissue heating is the primary mechanism underlying the biological effects of EM radiation; even minor temperature rises may disrupt cellular metabolism or tissue homeostasis. IEEE Standard C95.1 therefore adopts a 1 °C tissue temperature rise as a critical threshold, beyond which adverse effects such as cataract formation, blood–brain barrier permeability, and thermally induced tissue damage have been observed (Bailey et al., 2019).

The simulation parameters in the Ansys HFSS models are summarized here for reproducibility. The solution type was set to Driven Modal, and the antennas were excited using lumped ports with a reference impedance of 50 Ω. A discrete frequency sweep was employed. While the antenna and tissue model configurations are detailed in Sections 2.2, 2.3, respectively, the surrounding vacuum region was defined to extend at least 30 mm beyond all modeled

structures. The SAR computations followed the IEC/IEEE 62704–4 draft standard, with the voxel size fixed at 1 mm.

2.4.1 SAR assessment

The SAR distribution in tissue can be theoretically calculated using the following integral form:

$$\mathrm{SAR}(\mathbf{r}) = \frac{\sigma(\mathbf{r})|E(\mathbf{r})|^2}{\rho(\mathbf{r})} \tag{1}$$

where V and m represent the volume (in m^3) and the mass (in kg) of the exposed tissue region, respectively. $\rho(\mathbf{r})$ and $\sigma(\mathbf{r})$ denote the mass density (in kg/m^3) and electrical conductivity (in S/m) of the tissue at location $\mathbf{r}$. $E(\mathbf{r})$ is the root-mean-square (RMS) magnitude of the induced electric field (in V/m).

In this study, both the electric field and the SAR distribution were extracted from HFSS simulations. To comply with FCC and Canadian regulatory frameworks, all SAR values reported in this work refer to the peak spatial-average SAR computed over a cubic volume corresponding to 1 g of tissue.

2.4.2 Temperature rise assessment

The temperature evolution was governed by Pennes' bioheat equation (Pennes, 1948). When omitting blood perfusion and metabolic heat, the equation is simplified to the Fourier heat conducting equation (Narasimhan, 1999):

$$\rho(\mathbf{r})c(\mathbf{r})\frac{\partial T(\mathbf{r},t)}{\partial t} = \nabla \cdot [k(\mathbf{r})\nabla T(\mathbf{r},t)] + Q(\mathbf{r}), \tag{2}$$

where $T(\mathbf{r},t)$ is the transient tissue temperature, ρ is the tissue density in kg/m^3, c is the specific heat capacity in J/(kg·K), k is the thermal conductivity in W/(m·K). $Q(\mathbf{r}) = \rho(\mathbf{r}) \cdot \mathrm{SAR}(\mathbf{r})$ represents the volumetric heat source term induced by antenna radiation, where $\mathrm{SAR}(\mathbf{r})$ denotes the local SAR averaged over each 1 mm^3 voxel in the tissue models.

To apply Equation 2 to the multilayer tissue model, the computational domain was discretized into cubic voxels of 1 mm^3, ensuring both numerical stability and adequate resolution across tissue interfaces. Each voxel at location (i,j,k) was assigned the corresponding thermal properties $\rho_{i,j,k}$, $c_{i,j,k}$, and $k_{i,j,k}$ according to its tissue type, while the local SAR at (i,j,k) was denoted as $\mathrm{SAR}_{i,j,k}$.

Equation 2 was solved via an explicit finite-difference scheme:

$$T_{i,j,k}^{n+1} = T_{i,j,k}^n + \Delta t \left[\alpha_{i,j,k} \nabla^2 T_{i,j,k}^n + \frac{\mathrm{SAR}_{i,j,k}}{c_{i,j,k}} \right], \tag{3}$$

where $\alpha = k/(\rho c)$ is the thermal diffusivity in m^2/s, and ∇^2 denotes the 3D Laplacian operator discretized with central differences.
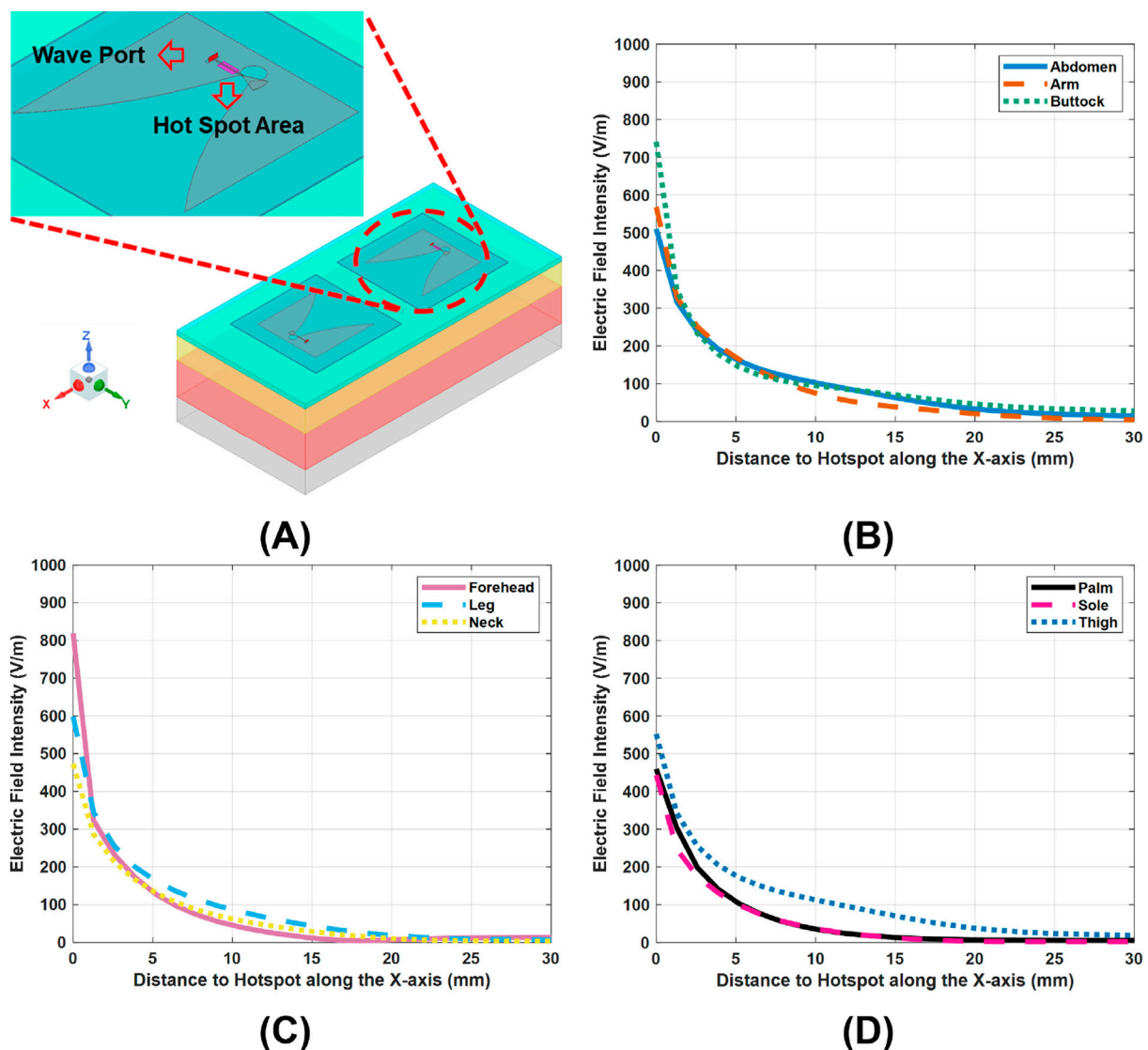
FIGURE 3
E-field variations across the nine tissue models, under a 10-dBm scans of the Vivaldi antennas. **(A)**, hot spot regions of electric field intensity, mark as pink. **(B–D)**, E-field distributions along the x-axis in the tissue models, with the hotspots set as the origins.

This approach allows for seamless modeling of parameter discontinuities across tissue layers without requiring special treatment at the interfaces. A Neumann (zero-flux) boundary conditions were imposed on all outer faces of the computational domain by setting the boundary temperature gradient to zero (Priya et al., 2013). The initial tissue temperature was set to 36.5 °C uniformly in the tissue models. A uniform spatial step of $\Delta x = \Delta y = \Delta z = 0.1$ mm was used to improve numerical stability, and the time step Δt was selected according to the three-dimensional Courant–Friedrichs–Lewy (CFL) stability criterion (De Moura and Kubrusly, 2013):

$$\Delta t \le \frac{1}{2\alpha_{\max}\left(\frac{1}{\Delta x^2} + \frac{1}{\Delta y^2} + \frac{1}{\Delta z^2}\right)}, \qquad (4)$$

where $\alpha_{\max}$ is the maximum diffusivity among all voxels.

The above scheme was implemented in MATLAB (Version 2024a). The 3D SAR array was directly imported from the HFSS simulation

results, and the tissue-type masks were used to assign ρ, c, and k to each voxel. At each time step, the Laplacian of the temperature field was computed via a 3D convolution kernel, and the temperature was updated according to the explicit scheme. The peak temperature rise in each tissue model was recorded as a function of exposure time.

3 Results

3.1 Vivaldi antenna

3.1.1 Electric field analysis

SAR is the primary metric for evaluating EM radiation safety. According to Equation 1, SAR is largely determined by the local electric field intensity E. Thus, examining the E-field distribution provides critical insight into where peak absorption occurs. Highlighted in pink in Figure 3A, the numerical simulations on a
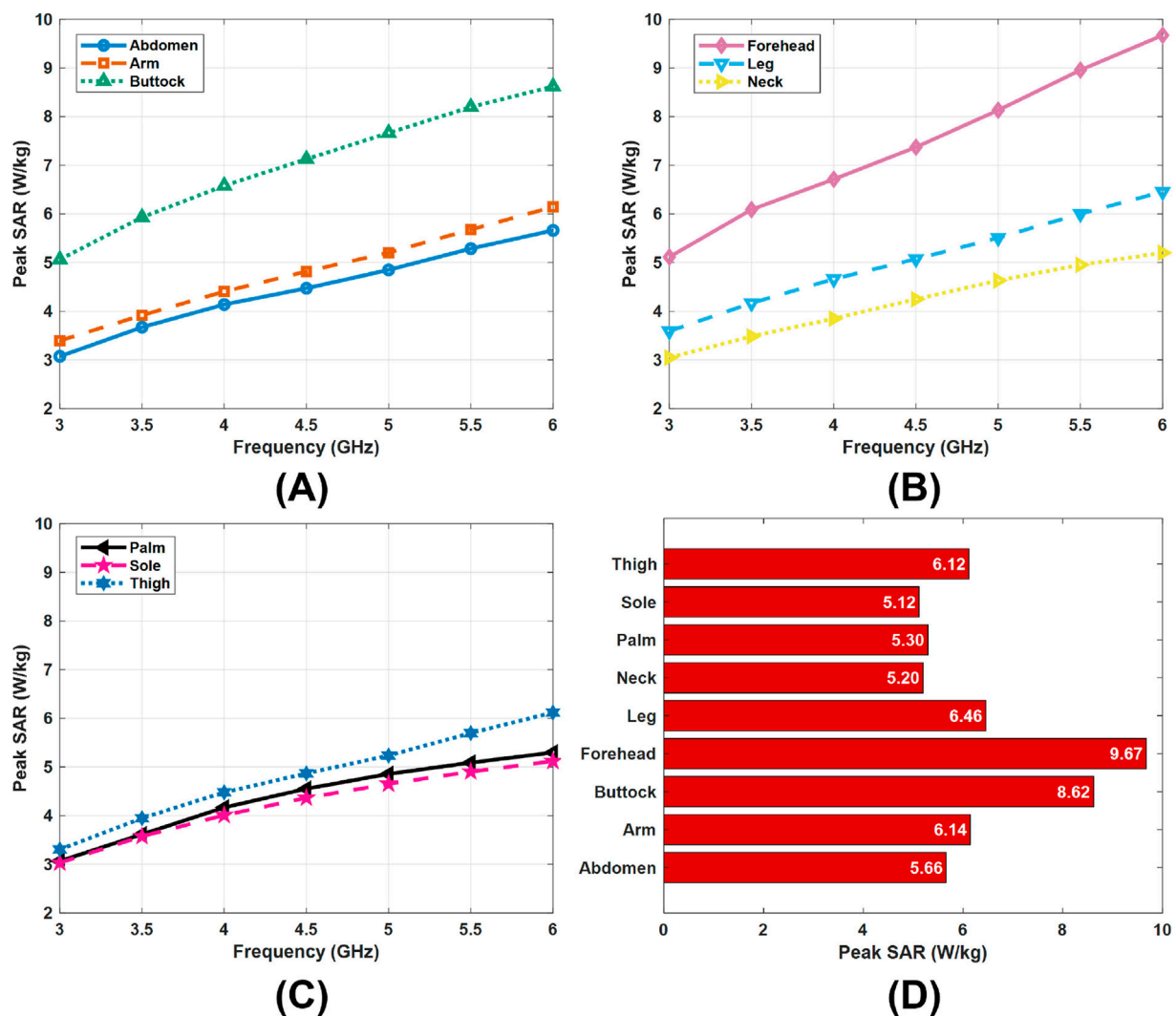
FIGURE 4
SAR variations across the tissue models under the Vivaldi antenna scans with 10 dBm input power. **(A–C)** SAR values at the hotspots across the 2−5 GHz frequency band in the tissue models. **(D)** Comparison of the peak SAR at 6 GHz among the tissue models.

10-dBm Vivaldi antenna scans reveal that for all nine tissue models, the peak E (the "hot spot") consistently appears in a small 2 mm × 6 mm area on the skin surface. This indicates that the SAR hot spot should be located at the skin surface and, importantly, coincides with the location of the E-field hot spot. In other words, the regions of strongest electric field on the skin correspond directly to the regions of highest energy absorption.
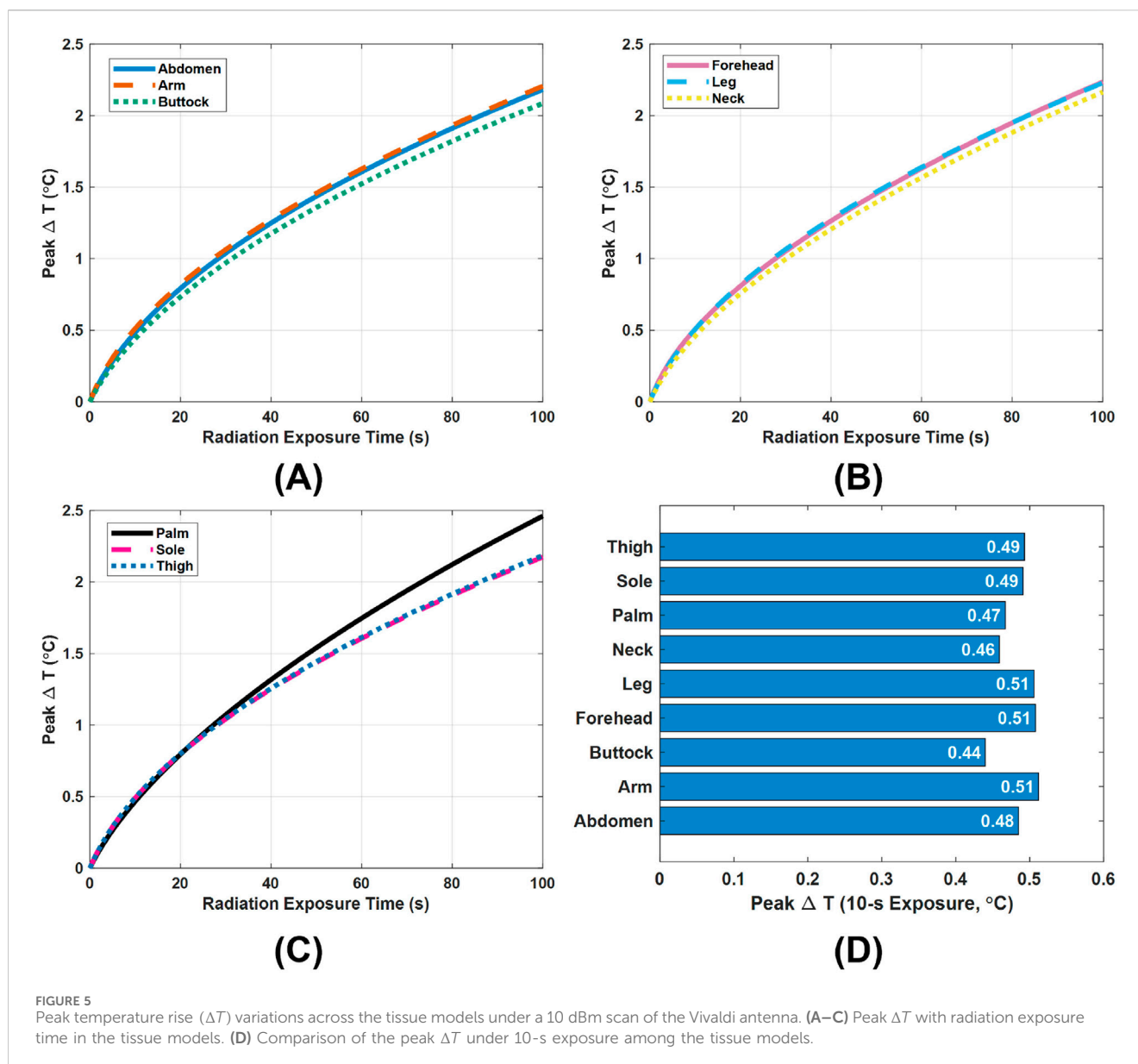
Indeed, variations across layers in electrical properties (conductivity σ and density ρ) may slightly distort how the SAR distribution aligns with the E-field distribution in depth. However, the E-field intensity attenuates exponentially with depth in tissue. The field strength diminishes so rapidly with distance that the σ or ρ differences are comparatively minor. Thus, the peak E at the surface still dictates the location of the peak SAR.

Figures 3B–D show the lateral E-field distribution between the antennas (along the x-axis) for each tissue model, with the hot spot at the origin. Consistent with theoretical expectations in (Shang et al., 2024; Shang et al., 2025), the E-field magnitude decays

approximately exponentially with distance away from the hot spot. Notably, the peak E-field differs greatly between models: it reaches about 820 V/m in the forehead model but only around 420 V/m in the sole model. This variation is attributed to differences in tissue model configuration. For example, the forehead has only 5.1 mm of soft tissue over bone, so the EM wave reflects strongly at the bone interface and constructively reinforces the field at the surface, yielding a higher local E-field. In contrast, other sites with much thicker soft tissue (about 11–33 mm) do not exhibit the same field enhancement, resulting in lower peak E at the surface.

3.1.2 SAR analysis

Figures 4A–C present the peak SAR values in the tissue models across the Vivaldi operating band (3–6 GHz) under an input power of 10 dBm. In all cases, the peak SAR exhibits a clear increasing trend with frequency. This frequency dependence can be explained by the dispersive nature of tissue dielectric properties. As frequency increases, the conductivity σ rises while the permittivity ε decreases. A higher

FIGURE 5
Peak temperature rise (ΔT) variations across the tissue models under a 10 dBm scan of the Vivaldi antenna. **(A−C)** Peak ΔT with radiation exposure time in the tissue models. **(D)** Comparison of the peak ΔT under 10-s exposure among the tissue models.
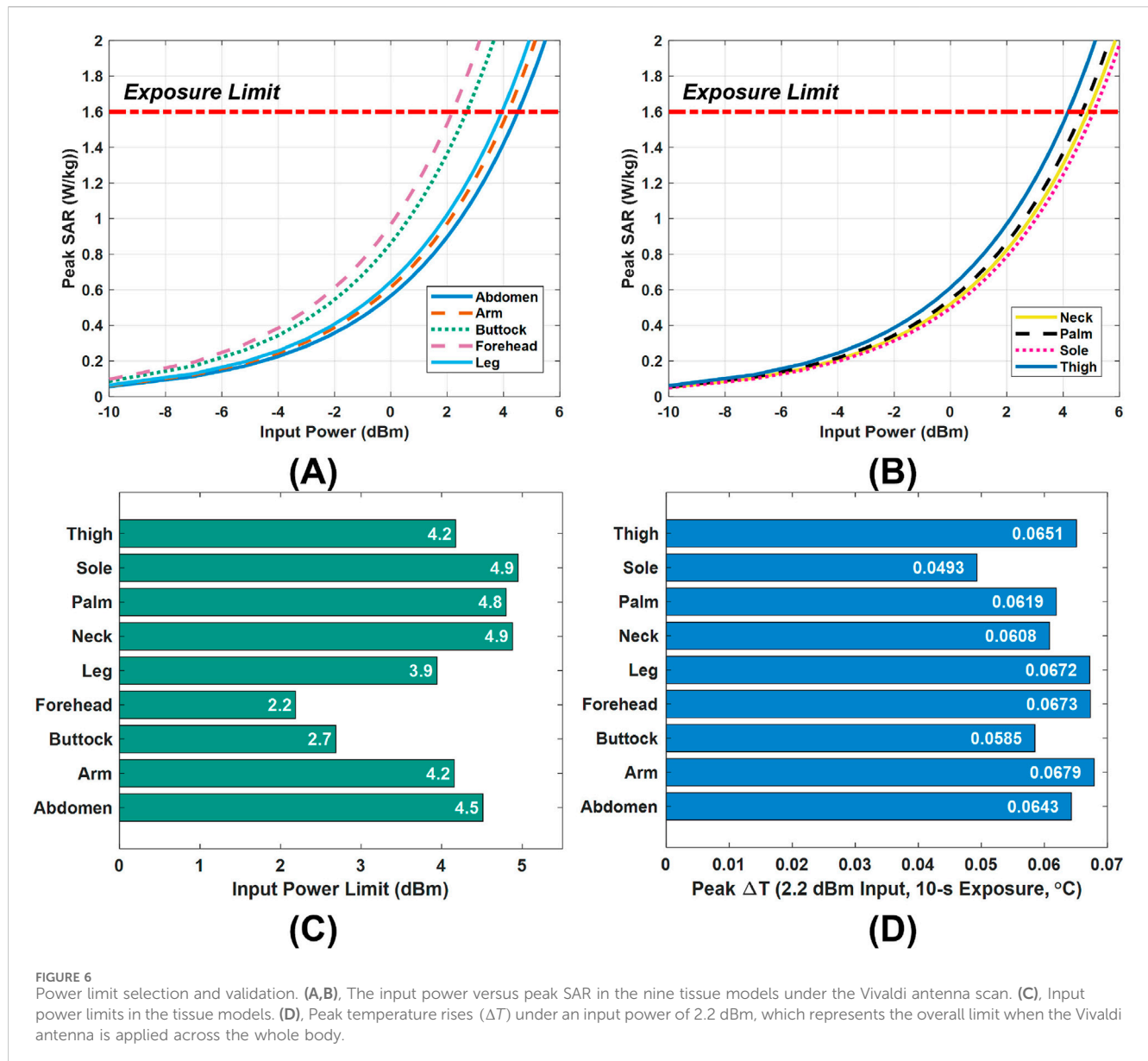
conductivity enhances the effective losses in tissue and strengthens the skin effect, thereby confining the EM field more tightly to the superficial layers where the hot spots occur. Because SAR is proportional to $\sigma|E|^2/\rho$, the combination of higher σ and surface-localized E-field leads to larger peak SAR at elevated frequencies.

More importantly, Figures 4A–C also reveal substantial differences among body sites. These differences persist across the entire frequency band. For instance, Figure 4D shows that at 6 GHz, the peak SAR in the forehead model approaches almost twice that in the sole or neck model, despite identical input power. Such differences arise from structural variations across body sites, such as differences in soft-tissue thickness, which can either amplify or attenuate the local E-field at the surface. Consequently, the resulting SAR values vary greatly between sites. These findings emphasize that radiation safety cannot be reliably assessed from a single anatomical model. Instead, the diversity of body sites and their distinct EM responses must be considered.

3.1.3 Temperature rises analysis

In addition to using SAR, evaluating the temperature rise (ΔT) caused by microwave exposure is crucial for antenna safety assessments. Using the theoretical model described in Section 2.4.2, we calculated the ΔT distribution in each tissue model for a given exposure duration. The peak ΔT over the tissue model represent the conservative worst-case condition. Figures 5A–C presents the peak ΔT attained in nine different tissue models under a 10-dBm Vivaldi antenna scan from 3 to 6 GHz (stepping by 0.1 GHz) over an exposure time of 100 s. It is noteworthy that such an exposure duration is much longer than the typical several-second period required for microwave-based skin cancer detection. However, analyzing the effect of extended exposure is essential to determine the maximum permissible exposure time of the antenna at a given power level, corresponding to the point where the temperature rise reaches the safety threshold. Significant variation among body sites is

FIGURE 6
Power limit selection and validation. **(A,B)**, The input power versus peak SAR in the nine tissue models under the Vivaldi antenna scan. **(C)**, Input power limits in the tissue models. **(D)**, Peak temperature rises (ΔT) under an input power of 2.2 dBm, which represents the overall limit when the Vivaldi antenna is applied across the whole body.

observed. For example, after 100 s of scanning, the palm model's peak ΔT reaches 2.47 °C, whereas in the buttock model it is about 20% lower. Furthermore, the peak ΔT at most body sites reaches the safety limit of 1 °C within 30 s, indicating that the selected transmission power of 10 dBm is excessively high.

In practice, however, a single scan of the designed Vivaldi or monopole antennas for skin cancer detection is very brief, typically lasting about 5–10 s depending on the frequency range and step size settings. Therefore, special attention must be paid to the peak ΔT that can occur during such short exposures. Figure 5D illustrates the peak ΔT in each tissue model for an exposure time of 10 s. Even in this short-exposure scenario, the inter-site differences remain pronounced. The highest 10-s temperature rise occurs in the arm model (0.516 °C), which is roughly 16% higher than the peak ΔT in the buttock model under the same conditions.

The above ΔT variations observed in both 10-s and 100-s exposures reaffirm the necessity of a comprehensive, full-body

analysis in antenna safety evaluations. In addition, a clear discrepancy is noted between the regions of highest SAR and the regions of highest ΔT among the various body sites. For instance, the buttock model exhibits the second-highest peak SAR of all the models (see Figure 4), yet it produces the smallest temperature rise. This inconsistency arises because ΔT is influenced not only by the hot spot of the SAR but also by spacial and time distribution of absorbed power in tissues, as well as the layers' thermal properties and energy diffusion. Given that tissue temperature rise is the direct cause of thermal damage, this finding highlights the limitations of relying solely on SAR-based analysis and the importance of ΔT-based assessments.

3.1.4 Power limit selection

Figures 6A,B illustrates the variation of peak SAR with input power across nine different tissue models, providing guidance for

TABLE 2 Variations of the key metrics across body sites in monopole antenna radiation safety analysis.

Body site	Peak $|E|$	Peak SAR (W/kg)				Peak ΔT
	(V/m)	2 GHz	3 GHz	4 GHz	5 GHz	(10-s exposure, ℃)
Abdomen	399.2	163.1	215.6	276.7	380.1	0.3300
Arm	499.4	172.8	249.0	296.2	396.4	0.2877
Buttock	420.0	154.0	230.8	334.6	465.5	0.3674
Forehead	538.7	326.8	534.6	654.6	824.1	0.2999
Leg	422.3	192.1	272.3	331.1	439.9	0.3046
Neck	416.5	171.0	221.9	280.3	360.3	0.3547
Palm	418.2	172.2	228.0	276.5	329.9	0.4654
Sole	420.8	191.2	231.1	279.1	340.3	0.3816
Thigh	405.1	161.1	235.7	306.3	419.8	0.3135

safe power selection. From these results, we derive a power limit for each model that still meets the 1.6 W/kg SAR criterion from FCC. The specific limits for all tissue models are summarized in Figure 6C. Consistent with the SAR variations by body site (see Figure 4), these allowable power levels vary widely among different locations, ranging from as low as 2.2 dBm for the forehead model up to 4.9 dBm for the sole model. In practice, this means the antenna's placement strongly influences the safe operating power. For instance, when the Vivaldi antenna is used at a particular body site, its input power can be set according to that site's specific limit. However, for general or full-body use, a conservative approach is adopted: the global input power limit should be the lowest of all local limits. In our case, this corresponds to 2.2 dBm (dictated by the forehead model), ensuring that the SAR remains below 1.6 W/kg in all exposure scenarios.

A temperature-rise simulation was performed to validate the safety of this 2.2 dBm global power limit. Figure 6D presents the peak tissue temperature increase after a 10-s exposure at 2.2 dBm input power. The observed highest value is only about 0.068 ℃, a negligible rise far below levels that would pose any health risk. This minimal heating is in line with the SAR limit compliance and indicates that the chosen power cap does not cause undue thermal stress. Therefore, adopting 2.2 dBm as the input power limit is confirmed to be a safe and reasonable choice.
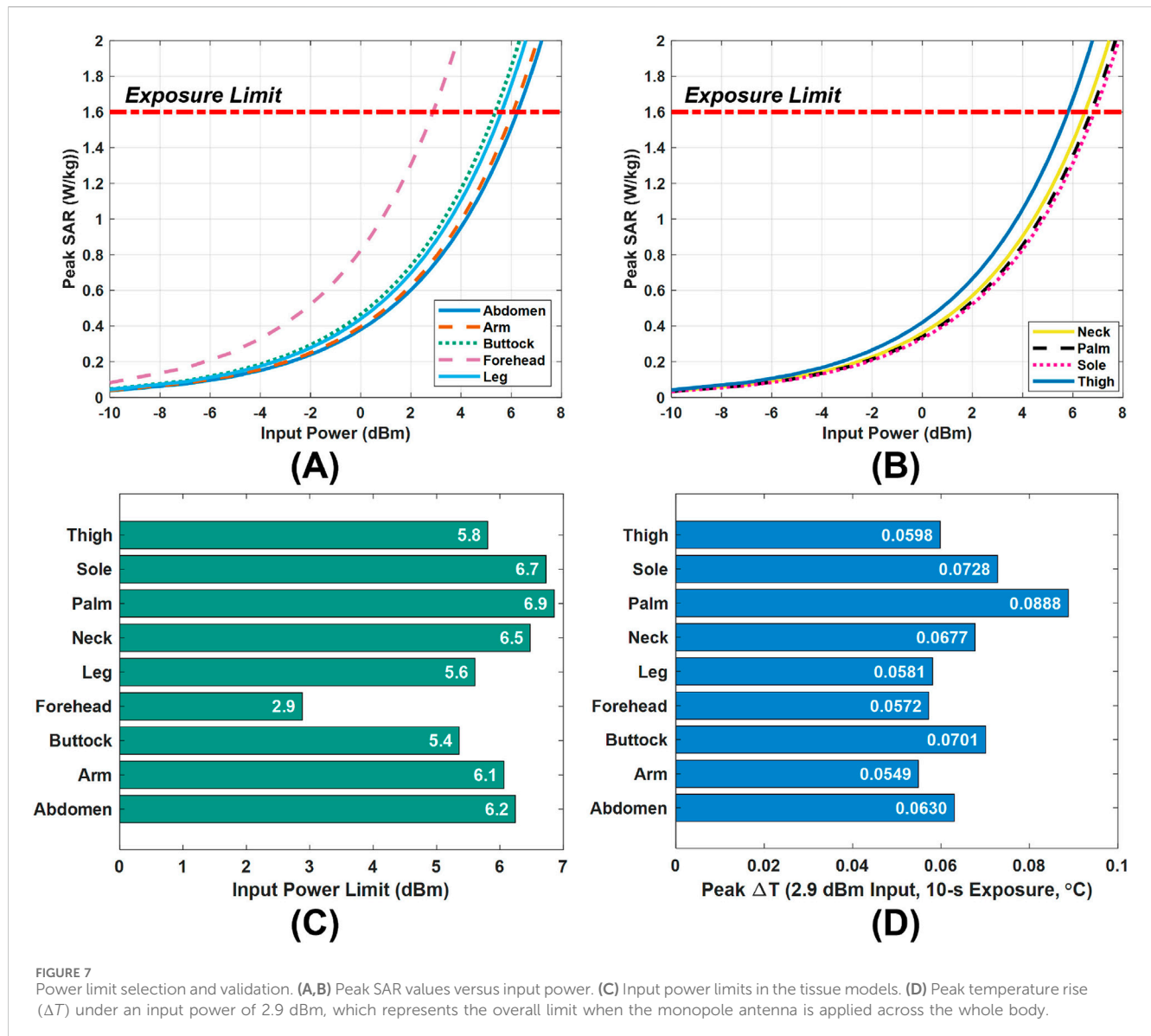
3.2 Monopole antenna

Following the same analysis methodology developed for the Vivaldi antenna, we evaluate the radiation safety of monopole antennas, which represent our first-generation design of the surface-wave antennas for skin cancer diagnosis. Table 2 summarizes the variations in key radiation metrics across nine body sites with the input power fixed at 10 dBm. The peak E-field distributions are similar to those observed for the Vivaldi antennas in Section 3.1.1. The hotspots, namely the locations of the peak E in the tissue models, appear on the top surface of the skin layers, directly beneath the SMA port of

the transmitting antenna. The body sites exhibiting the highest and lowest peak E values are consistent with the Vivaldi antenna results: the highest, 538.7 V/m, occurs in the forehead model, while the lowest, 399 V/m, is found in the sole model. The peak SAR results among the body sites follow the trend in E-field. The forehead model exhibits the highest peak SAR across the 2–5 GHz band owing to its very thin soft-tissue structure. All other sites show 43%–54% lower peak SAR. These pronounced differences in reinforce that safety assessments should incorporate multiple body site models rather than rely on a single reference site.

In addition to field and SAR metrics, Table 2 also lists the peak temperature rise ΔT for each site when the monopole antennas repeatedly scan from 2 to 5 GHz (0.1 GHz step) over a 10 s exposure. The largest peak ΔT occurs in the palm (0.4654 ℃), while the forehead shows the smallest increase (0.2999 ℃). Notably, the ranking of peak ΔT differs from that of peak $|E|$ and SAR, reflecting the additional influence of tissue thermal properties and heat conduction. Because temperature elevation, not SAR alone, ultimately determines thermal hazard, these discrepancies emphasize the necessity of including temperature-rise analysis in comprehensive safety evaluations.

Figures 7A,B show the peak SAR values obtained for the monopole antenna, which are used to determine the maximum transmit power that complies with the FCC's 1.6 W/kg SAR limit. Figure 7C summarizes the corresponding power limits at each examined body site under conservative worst-case conditions. Among all sites, the forehead has the most restrictive allowable power (2.9 dBm). Therefore, when the monopole antenna is intended for use across the entire body, rather than at a single specific site, 2.9 dBm is chosen as a global power limit to ensure compliance at all locations. It is our recommendation that similar analysis be followed for any antenna-like sensor.

To validate the safety of this global limit, a thermal analysis was conducted by exposing the tissue models to a continuous 10-s scan at 2.9 dBm. Figure 7D presents the resulting temperature rise in tissues. Even at the most affected location (the palm), the peak

FIGURE 7
Power limit selection and validation. **(A,B)** Peak SAR values versus input power. **(C)** Input power limits in the tissue models. **(D)** Peak temperature rise (ΔT) under an input power of 2.9 dBm, which represents the overall limit when the monopole antenna is applied across the whole body.

temperature increase remains below 0.09 °C, a negligible rise that poses no health concern.

4 Conclusion and discussion

This work presented a site-dependent radiation-safety assessment of surface-wave antennas by multiple thermal metrics analysis. Full-wave simulations on nine multilayer tissue models showed significant inter-site variability in peak SAR and temperature increase (ΔT), implying the need for full-body assessment. The ranking of peak ΔT across sites does not necessarily follow that of the SAR, underscoring the limitations of SAR-only analyses and the importance of incorporating ΔT. Based on the 1.6 W/kg criterion, we derived local and global input-power limits for the two antennas and verified their conservativeness via short-exposure thermal analysis.

The two antenna designs, the Vivaldi and monopole structures, exhibited highly consistent spatial patterns in electric-field distribution

and SAR ranking across the examined body sites. Although their working frequency bands are not identical, both antennas produced similar inter-site trends: the forehead model showed the highest field intensity and peak SAR, while the sole model exhibited the lowest values. This similarity supports the general applicability of the proposed evaluation framework for wearable sensors.

The bio-heat formulation used in this study did not include blood perfusion, metabolic heat, and convective cooling at the skin–air interface, which may result in conservative (overestimated) temperature predictions. These simplifications were made with awareness that we are establishing an upper bound for thermal safety. Future work will incorporate perfusion and heterogeneous boundary effects for completeness.

More generally, the present study suggests a standardized methodology for radiation-safety analysis of the microwave devices aimed at healthcare. The proposed workflow, from electric-field mapping and SAR calculation to temperature-rise evaluation and power-limit derivation, offers a comprehensive

framework that bridges electromagnetic design and biomedical safety considerations.

Data availability statement

The original contributions presented in the study are included in the article/supplementary material, further inquiries can be directed to the corresponding author.

Author contributions

SS: Conceptualization, Data curation, Formal Analysis, Investigation, Methodology, Software, Visualization, Writing – original draft, Writing – review and editing, Validation. MP: Conceptualization, Formal Analysis, Funding acquisition, Investigation, Project administration, Resources, Supervision, Writing – review and editing.

Funding

Conflict of interest

The authors declare that the research was conducted in the absence of any commercial or financial relationships that could be construed as a potential conflict of interest.

Generative AI statement

The authors declare that no Generative AI was used in the creation of this manuscript.

Any alternative text (alt text) provided alongside figures in this article has been generated by Frontiers with the support of artificial intelligence and reasonable efforts have been made to ensure accuracy, including review by the authors wherever possible. If you identify any issues, please contact us.

Publisher's note

All claims expressed in this article are solely those of the authors and do not necessarily represent those of their affiliated organizations, or those of the publisher, the editors and the reviewers. Any product that may be evaluated in this article, or claim that may be made by its manufacturer, is not guaranteed or endorsed by the publisher.

References

Alemaryeen, A., and Noghanian, S. (2023). A survey of the thermal analysis of implanted antennas for wireless biomedical devices. *Micromachines* 14, 1894. doi:10.3390/mi14101894

Angin, S., Crofts, G., Mickle, K. J., and Nester, C. J. (2014). Ultrasound evaluation of foot muscles and plantar fascia in pes planus. *Gait and Posture* 40, 48–52. doi:10.1016/j.gaitpost.2014.02.008

Bahramiabarghouei, H., Porter, E., Santorelli, A., Gosselin, B., Popovic, M., and Rusch, L. A. (2015). Flexible 16 antenna array for microwave breast cancer detection. *IEEE Trans. Biomed. Eng.* 62, 2516–2525. doi:10.1109/TBME.2015.2434956

Bailey, W. H., Bodemann, R., Bushberg, J., Chou, C.-K., Cleveland, R., Faraone, A., et al. (2019). Synopsis of ieee std c95. 1™-2019 "ieee standard for safety levels with respect to human exposure to electric, magnetic, and electromagnetic fields, 0 hz to 300 ghz". *IEEE Access* 7, 171346–171356. doi:10.1109/access.2019.2954823

Choi, Y.-J., Lee, K.-W., Gil, Y.-C., Hu, K.-S., and Kim, H.-J. (2019). Ultrasonographic analyses of the forehead region for injectable treatments. *Ultrasound Medicine and Biology* 45, 2641–2648. doi:10.1016/j.ultrasmedbio.2019.06.414

Christ, A., Klingenbock, A., Samaras, T., Goiceanu, C., and Kuster, N. (2006). The dependence of electromagnetic far-field absorption on body tissue composition in the frequency range from 300 mhz to 6 ghz. *IEEE Trans. Microw. Theory Tech.* 54, 2188–2195. doi:10.1109/TMTT.2006.872789

Costanzo, S., Flores, A., and Buonanno, G. (2023). Fast and accurate cnn-based machine learning approach for microwave medical imaging in cancer detection. *IEEE Access* 11, 66063–66075. doi:10.1109/access.2023.3291076

De Moura, C. A., and Kubrusly, C. S. (2013). The courant–friedrichs–lewy (cfl) condition. *AMC* 10, 45–90. doi:10.1007/978-0-8176-8394-8

Demers, P., Findlay, D., Foster, K. A., Kolb, B., Moulder, J., Nicol, A.-M., et al. (2014). *A review of safety code 6 (2013): Health canada's safety limits for exposure to radiofrequency fields*. Canada Ottawa: Royal Society of.

Fields, R. E. (1997). Evaluating compliance with fcc guidelines for human exposure to radiofrequency electromagnetic fields. *Oet Bull.* 65, 1–57. Available online at: https://transition.fcc.gov/Bureaus/Engineering_Technology/Documents/bulletins/oet65/oet65c.pdf.

Gniadecka, M., Nielsen, O. F., and Wulf, H. C. (2003). Water content and structure in malignant and benign skin tumours. *J. Mol. Struct.* 661, 405–410. doi:10.1016/j.molstruc.2003.08.030

Griffin, N. L., and Richmond, B. G. (2005). Cross-sectional geometry of the human forefoot. *Bone* 37, 253–260. doi:10.1016/j.bone.2005.04.019

Haider, Z., Le Drean, Y., Sacco, G., Nikolayev, D., Sauleau, R., and Zhadobov, M. (2022). High-resolution model of human skin appendages for electromagnetic dosimetry at millimeter waves. *IEEE J. Microwaves* 2, 214–227. doi:10.1109/JMW.2021.3126712

IFAC – CNR (2024). Istituto di Fisica Applicata 'Nello Carrara. Available online at: http://www.ifac.cnr.it/ (Accessed April 14, 2025).

IT'IS Foundation (2025). IT'IS foundation - database of tissue properties. Available online at: http://itis.swiss/virtual-population/tissue-properties/database (Accessed August 10, 2025).

Kaur, K., Arif, A., and Ahmad, A. (2022). In vitro detection of skin cancer using a uwb stacked microstrip patch antenna with microwave imaging. *Int. J. RF Microw. Computer-Aided Eng.* 32, e23188. doi:10.1002/mmce.23407

Kaur, K., Arif, A., and Ahmad, A. (2024). *In silico,*, *in vitro,*, and *in vivo* validation of a microwave imaging system for early skin cancer detection. *Int. J. Imaging Syst. Technol.* 30, e23016. doi:10.1002/ima.23016

Kodera, S., Taguchi, K., Diao, Y., Kashiwa, T., and Hirata, A. (2024). Computation of whole-body average sar in realistic human models from 1 to 100 ghz. *IEEE Trans. Microw. Theory Tech.* 72, 91–100. doi:10.1109/TMTT.2023.3289562

Lee, Y., and Hwang, K. (2002). Skin thickness of Korean adults. *Surg. Radiologic Anatomy* 24, 183–189. doi:10.1007/s00276-002-0034-5

Mirzaee, M., Ma, X., Rahman, M. T., and Noghanian, S. (2021). "Early skin cancer detection: from desktop imaging setup to real-time handheld device," in *IEEE MTT-S international microwave symposium (IMS)* (IEEE), 216–219.

Mokhtari, M., and Popović, M. (2025). "Surface-wave skin characterization with a flexible vivaldi antenna," in *2025 19th European conference on antennas and propagation (EuCAP)* (IEEE), 1–5.

Morgan, D., Spiers, F., Pulvertaft, C., and Fourman, P. (1967). The amount of bone in the metacarpal and the phalanx according to age and sex. *Clin. Radiol.* 18, 101–108. doi:10.1016/s0009-9260(67)80137-5

Morimoto, A., Suga, T., Tottori, N., Wachi, M., Misaki, J., Tsuchikane, R., et al. (2017). Association between hand muscle thickness and whole-body skeletal muscle mass in healthy adults: a pilot study. *J. Physical Therapy Science* 29, 1644–1648. doi:10.1589/jpts.29.1644

Naqvi, S. A. R., Mobashsher, A. T., Mohammed, B., Foong, D., and Abbosh, A. (2024). Handheld microwave system for *in vivo* skin cancer detection: development and clinical validation. *IEEE Trans. Instrum. Meas.* 73, 1–16. doi:10.1109/tim.2024.3398123

Naqvi, S. A. R., Rajmohan, I. J., Xue, F., Foong, D., and Abbosh, A. (2025). Electromagnetic techniques and systems for non-invasive skin cancer detection and classification: current status and future perspectives. *IEEE Trans. Instrum. Meas.* 74, 1–24. doi:10.1109/tim.2025.3604920

Narasimhan, T. N. (1999). Fourier's heat conduction equation: history, influence, and connections. *Rev. Geophys.* 37, 151–172. doi:10.1029/1998rg900006

Pennes, H. H. (1948). Analysis of tissue and arterial blood temperatures in the resting human forearm. *J. Applied Physiology* 1, 93–122. doi:10.1152/jappl.1948.1.2.93

Priya, G. S., Prakash, P., Nieto, J., and Kayar, Z. (2013). Higher-order numerical scheme for the fractional heat equation with dirichlet and neumann boundary conditions. *Numer. Heat. Transf. Part B Fundam.* 63, 540–559. doi:10.1080/10407790.2013.778719

Roky, A. H., Islam, M. M., Ahasan, A. M. F., Mostaq, M. S., Mahmud, M. Z., Amin, M. N., et al. (2025). Overview of skin cancer types and prevalence rates across continents. *Cancer Pathogenesis Therapy* 3, 89–100. doi:10.1016/j.cpt.2024.08.002

Rowbotham, S. K., Mole, C. G., Tieppo, D., Blaszkowska, M., Cordner, S. M., and Blau, S. (2023). Average thickness of the bones of the human neurocranium: development of reference measurements to assist with blunt force trauma interpretations. *Int. Journal Legal Medicine* 137, 195–213. doi:10.1007/s00414-022-02824-y

Sacco, G., Haider, Z., and Zhadobov, M. (2022). Exposure levels induced in curved body parts at mmwaves. *IEEE J. Electromagn. RF Microwaves Med. Biol.* 6, 413–419. doi:10.1109/JERM.2022.3178604

Schiavoni, R., Maietta, G., Filieri, E., Masciullo, A., and Cataldo, A. (2023). Microwave reflectometry sensing system for low-cost *in-vivo* skin cancer diagnostics. *IEEE Access* 11, 13918–13928. doi:10.1109/access.2023.3243843

Shang, S., Mokhtari, M., Tchinov, M., and Popović, M. (2024). "Employing surface waves for detection of skin melanoma: initial analysis and simulations," in *2024 IEEE MTT-S international microwave biomedical conference* (Montreal, QC, Canada IMBioC), 96–98. doi:10.1109/IMBioC60287.2024.10590463

Shang, S., Mokhtari, M., and Popović, M. (2025). Employing surface waves for characterizing skin: experimental validation. *IEEE J. Electromagn. RF Microwaves Med. Biol.* 9, 110–116. doi:10.1109/JERM.2025.3555198

Störchle, P., Müller, W., Sengeis, M., Lackner, S., Holasek, S., and Fürhapter-Rieger, A. (2018). Measurement of mean subcutaneous fat thickness: eight standardised ultrasound sites compared to 216 randomly selected sites. *Sci. Reports* 8, 16268. doi:10.1038/s41598-018-34213-0

Suryanata, F. A., Muhammad, N. F., Azizi, N. N. A. A., Dewan, R., and Roy, B. (2023). Performance analysis of wearable antenna worn in close proximity with human body. *J. Med. Device Technol.* 2, 43–49. doi:10.11113/jmeditec.v1n1.28

Wu, J., and Liu, J. (2024). Review of the capacity to accurately detect the temperature of human skin tissue using the microwave radiation method. *Biosensors* 14, 221. doi:10.3390/bios14050221